ACS APPLIED ELECTRONIC MATERIALS

pubs.acs.org/acsaelm

Article

# THz Thin Film Varactor Based on Integrated Ferroelectric $HfZrO_2$

Sukhrob Abdulazhanov,* Quang Huy Le, Dang Khoa Huynh, Defu Wang, David Lehninger, Thomas Kämpfe, and Gerald Gerlach*

Cite This: *ACS Appl. Electron. Mater.* 2023, 5, 189−195

Read Online

ACCESS | Metrics & More | Article Recommendations | Supporting Information

**ABSTRACT:** In this paper, we present a broadband microwave characterization of ferroelectric hafnium zirconium oxide ($Hf_{0.5}Zr_{0.5}O_2$) metal−ferroelectric−metal (MFM) thin film varactor from 1 kHz up to 0.11 THz. The varactor is integrated into the back-end-of-line (BEoL) of 180 nm CMOS technology as a shunting capacitor for the coplanar waveguide (CPW) transmission line. At low frequencies, the varactor shows a slight imprint behavior, with a maximum tunability of 15% after the wake-up. In the radio- and mmWave frequency range, the varactor's maximum tunability decreases slightly from 13% at 30 MHz to 10% at 110 GHz. Ferroelectric varactors were known for their frequency-independent, linear tunability as well as low loss. However, this potential was never fully realized due to limitations in integration. Here, we show that ferroelectric $HfO_2$ thin films with good back-end-of-line compatibility support very large scale integration. This opens up a broad range of possible applications in the mmWave and THz frequency range such as 6G communications, imaging radar, or THz imaging.

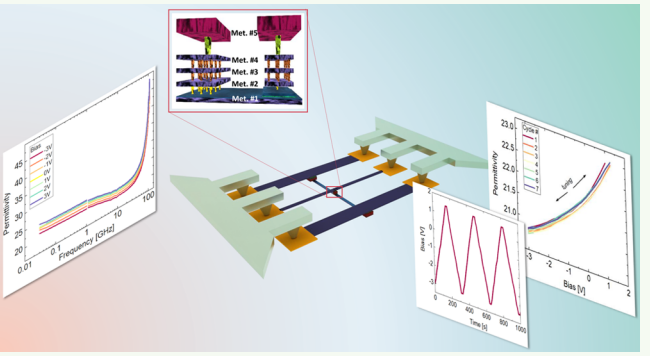


**KEYWORDS:** *BEoL, varactor, ferroelectric, HZO, tunability, loss tangent, de-embedding, VNA*

## INTRODUCTION

Ferroelectric materials are widely used in RF and mmWave applications as tunable devices. Due to their high dielectric permittivity, they are providing low-loss operation at frequencies above 20 GHz, where they outperform conventional dielectric materials. The most exploited ferroelectrics so far are perovskite-based ferroelectrics, like barium strontium titanate (BST) and lead zirconium titanate (PZT), that have high tuning properties and low dielectric losses. More recently, hafnium oxide ($HfO_2$) has gained a lot of interest since the discovery of its ferroelectricity.[1] The main research focus has been based on exploiting the use for nonvolatile memories like ferroelectric field effect transistors (FeFETs). Recently, it has been shown that the integration of ferroelectric $HfO_2$ in the back-end-of-line (BEoL) as a high-$k$ ferroelectric capacitor is feasible also in advanced node CMOS technologies.[2] The ferroelectric can change its permittivity upon applied bias and performs as a varactor.[3] In comparison to the BST and PZT varactors, the main advantage of ferroelectric $HfO_2$ is its low annealing temperature, good manufacturing properties for etching and deposition, and low tuning voltages, which makes it perfectly compatible with advanced CMOS node implementation and hence will make it now possible to design much higher frequency varactor-tuned low-power millimeter wave systems such as needed for 6G communications, imaging radar, or THz imaging. When doped with Zr with a 1:1 doping ratio, resulting $Hf_{0.5}Zr_{0.5}O_2$ ferroelectricity can be obtained at 400 °C,[3,4] which facilitates the integration of the varactor into the back-end-of line of CMOS processes.

The high-frequency characterization of ferroelectric hafnium oxide thin films was a topic of different research groups up to microwave frequencies.[5−9] The possible use for varactor implementations up to millimeter wave frequencies was predicted from simulation.[10,11] Previously, the wide-band characterization of dielectric $HfO_2$ thin films has been intensively investigated. However, not a clear consensus could be drawn for millimeter wave frequencies. Some of the studies claimed the presence of dielectric relaxation already at sub-GHz frequencies,[12−15] while others did not reveal the decrease of permittivity up to 20 GHz.[16] Our simulations predict inaccuracies in the device fixture for this uncertainty. For example, in a previous study we applied the annular ring method, with which we were able to extract the capacitance−voltage ($C$−$V$) characteristics up to 0.5 GHz.[8] But due to the imperfectness of the extraction and due to the inhomogeneous distribution of electric fields on bottom thin film TiN

**Received:** September 22, 2022
**Accepted:** November 14, 2022
**Published:** December 23, 2022

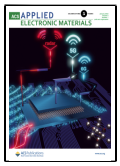

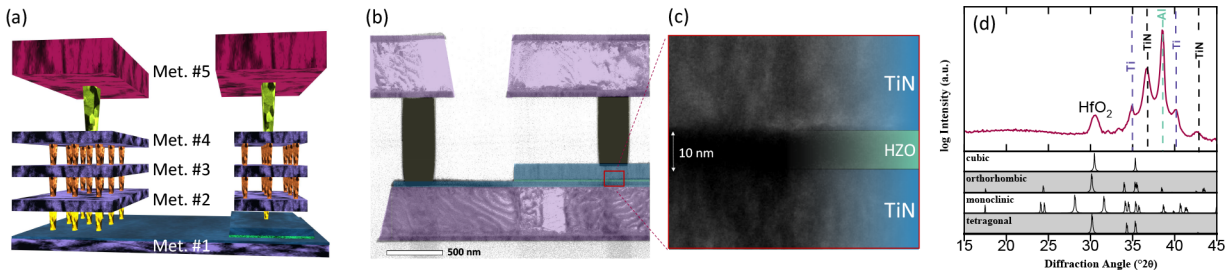


**Figure 1.** BEoL integration scheme of the MFM varactor into the 180 nm CMOS SOI technology (a), transmission electron microscopy of the MFM varactor placed between metals #2 and #3 (b) and the MFM stack (c), and the XRD analysis of the MFM stack (d).

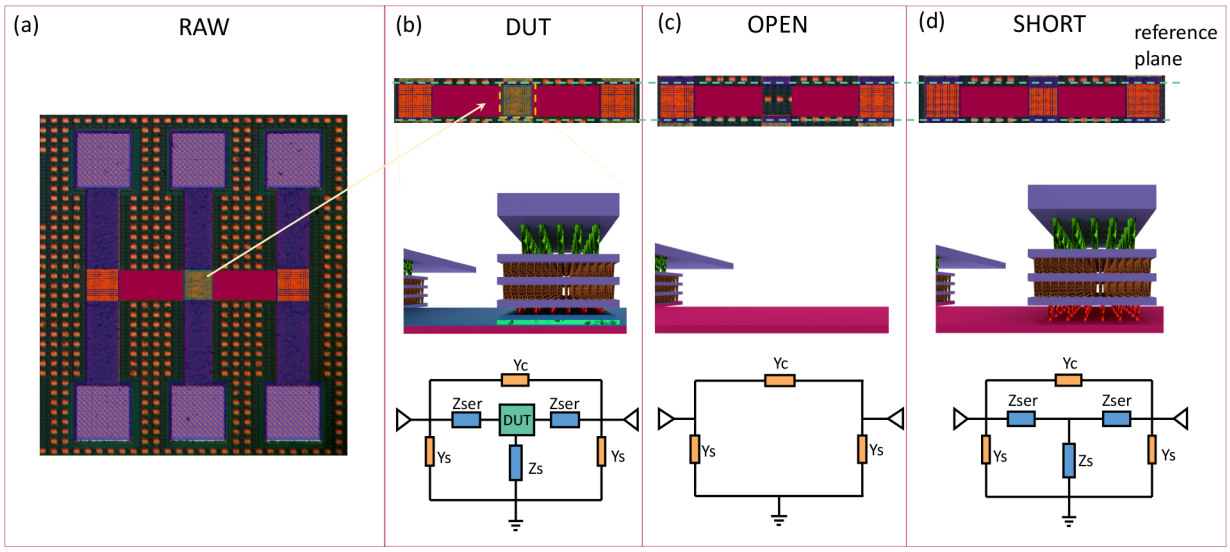


**Figure 2.** Microscopy image of the test structure for RF characterization (a); the 3D illustration and the schematics of the DUT (b), OPEN (c), and SHORT (d) de-embedding structures with a reference plane located in the vicinity of the varactor.

electrodes at high frequencies, which is similar to the well-known skin effect, both the permittivity and tunability appear to be decreasing at frequencies higher than 0.5 GHz. So far, the highest frequency up to which the dielectric $HfO_2$ was characterized with proper high-frequency fixture by using a coplanar waveguide (CPW) transmission line was 20 GHz.[16] By using a CPW the parasitics were extracted by de-embedding. This study gave proof that dielectric relaxation is not affecting $HfO_2$ thin films up to the high microwave frequency range. In this paper we present the characterization of hafnium zirconium oxide (HZO) thin film capacitors integrated into a CPW, using the OPEN−SHORT de-embedding technique. We were able to extract the tuning in permittivity at frequencies up to 110 GHz, which, to the authors' knowledge, is by far the highest frequency at which this material has been characterized. A constant tuning of these thin films was observed, which shows that they can be applied as varactors for millimeter-wave applications.

## FABRICATION

The fabrication of the HZO varactors was carried out in the BEoL section of a 180 nm HV SOI CMOS technology. The whole stack, hereby, consists of five metal layers [Figure 1(a)], where the thin film ferroelectric varactor was integrated as a standard metal−insulator−metal (MIM) capacitor between the Met.#2 and Met.#3 metallization layers [Figure 1(b)]. The metal−ferroelectric−metal (MFM) stack consists of Zr-doped $HfO_2$ with a 1:1 Hf:Zr doping ratio and a 10 nm thickness [Figure 1(c)], deposited on top of a TiN layer, that acts as diffusion barrier for the AlCu electrodes. The top TiN film is deposited on top of HZO to facilitate the formation of the ferroelectric phase.

In Figure 1(d) X-ray diffraction (XRD) of the phase is presented, in which the characteristics peaks of the orthorhombic/tetragonal phase are observable at 30°. Also a small content of the monoclinic phase is evident from the peak at 32°.

The topology of the test structures is based on a CPW transmission line [Figure 2(a)], with a lumped shunting varactor in the center. For the broadband RF/mmWave characterization the varactors with different areas, suitable for different frequencies, were deposited (see Supporting Information). The varactor device area was varied between 4 and 900 $\mu m^2$ for high- and low-frequency characterization, respectively.

For the proper extraction of the varactor capacitance and compensation of the parasitics, the OPEN−SHORT de-embedding was implemented[17] [Figure 2(b)−(d)]. A more detailed explanation of the applied de-embedding technique is presented in the Supporting Information.

## EXPERIMENTAL SETUP

Low-frequency electrical characterization of the varactors was performed on an aixACCT TF analyzer 3000, which uses the virtual ground method[18] for dynamic hysteresis measurement, where the electric field waveform is applied to the sample and the corresponding


https://doi.org/10.1021/acsaelm.2c01273
ACS Appl. Electron. Mater. 2023, 5, 189−195

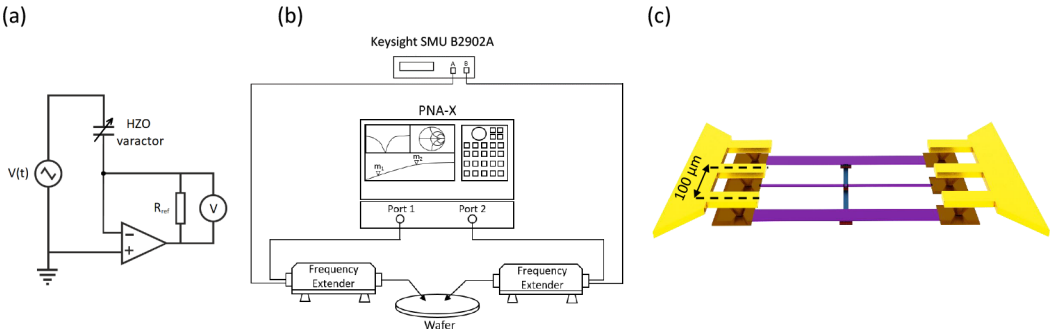


**Figure 3.** Schematic of the low-frequency characterization (a) using an aixACCT TF analyzer 3000 and of the mmWave characterization (b) using a Keysight N5247B PNA-X VNA with 100 $\mu$m GSG Infinity probes (c).

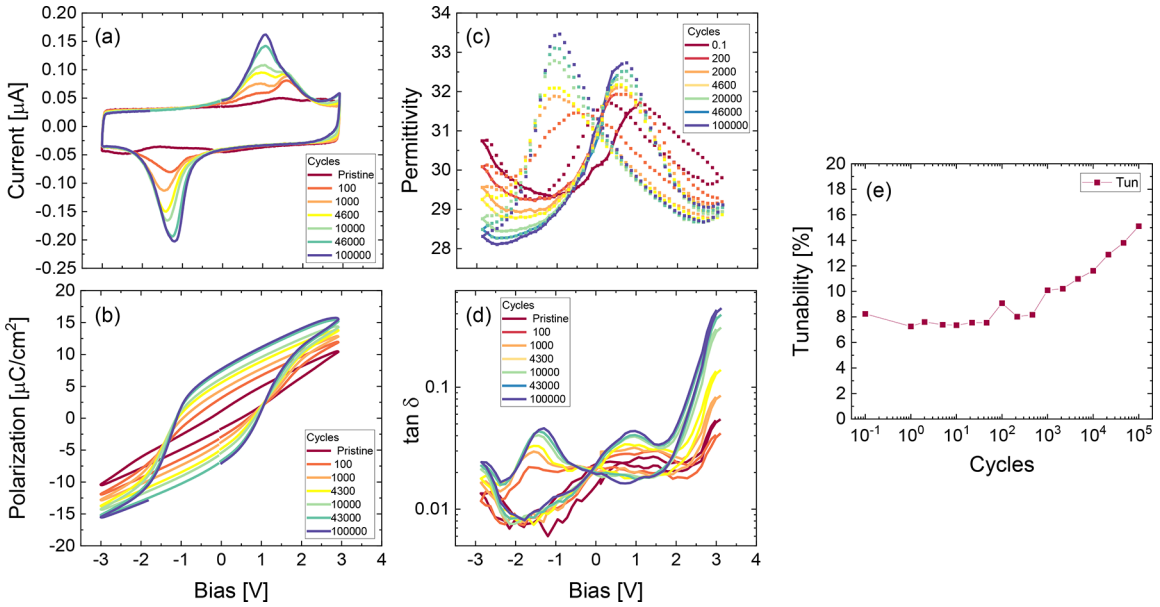


**Figure 4.** Low-frequency current−voltage ($I$−$V$) (a), polarization−voltage ($P$−$V$) (b), capacitance−voltage ($C$−$V$) (c), loss tangent−voltage (tan $\delta$−$V$) (d) characteristics, and the tunability (e) of the MFM varactor upon electric field cycling, experiencing a wake-up effect.

displacement current is measured though the operational amplifier [Figure 3(a)] and later integrated with time for polarization calculation. The polarization−voltage ($P$−$V$) characteristics were measured using a 1 kHz AC signal of 3 V amplitude with a triangular waveform. The low-frequency capacitance−voltage ($C$−$V$) characteristics were measured by integrating with time a small-amplitude (50 mV) sinusoidal AC signal of 1 kHz frequency, during the variation of the bias voltage ($V_b$) between −3 and 3 V.

The RF measurements were carried out on a Keysight N5247B PNA-X vector network analyzer [Figure 3(b)] with N5293A extender heads in the frequency range between 30 MHz and 110 GHz applying a −15 dBm signal. The 100 $\mu$m pitch ground−signal−ground (GSG) Infinity probes were used to contact the pads [Figure 3(c)]. For the capacitance tuning, the DC bias was applied upon RF signal by an SMU B2902A using the bias tee, integrated into the extenders. The RF measurements were performed both in the pristine state and after cycling with a 1 kHz square signal of 3 V amplitude for 100 000 times.

## ■ ELECTRICAL CHARACTERIZATION

In Figure 4 the basic low-frequency characteristics are presented. The current−voltage ($I$−$V$) characteristics and the polarization−voltage ($P$−$V$) characteristics with a distinguishing hysteresis loop are shown in Figure 4(a) and (b), respectively. The peak on the $I$−$V$ curve is due to displacement currents at the corresponding coercive voltage ($V_c$). The pristine $I$−$V$ and $P$−$V$ curves show a pinched behavior, which manifests itself in two distinct displacement current peaks, i.e., antiferroelectric-like behavior.[3] Additionally an imprint is present, evident from the peaks' displacement toward higher potential. Upon electric field cycling with ±3 V, the HZO undergoes a "wake-up" effect, expressed as an increase of the ferroelectric (FE) behavior, which in turn is manifested in increasing of the peaks' amplitude and removal of the pinching and partial removal of the imprint, which in turn results in the conventional ferroelectric shape of the $P$−$V$ curve. At later stages of the cycling, after approximately 100 000 cycles the arising leakage current peaks are observable at 3 V [Figure 4(a)] that result in the rounding of the $P$−$V$ flanks.

In Figure 4(c), a small-signal capacitance−voltage ($C$−$V$) characterization is shown, with the extracted permittivity of the HZO. The $C$−$V$ curve has a distinctive butterfly shape with peaks located at $V_c$, whose origin is considered the movement of ferroelectric domains upon bias sweep. On the pristine $C$−$V$ curve the peaks are broadened due to the pinching, similarly to $I$−$V$ peaks. Better visualization of pinched $C$−$V$ characteristics and of pinch removal upon cycling is presented in our previous work.[3] The $C$−$V$ characteristics also show an imprint behavior, similar to that observed in Figure 4(a), which is not fully removed upon cycling.



https://doi.org/10.1021/acsaelm.2c01273
ACS Appl. Electron. Mater. 2023, 5, 189−195

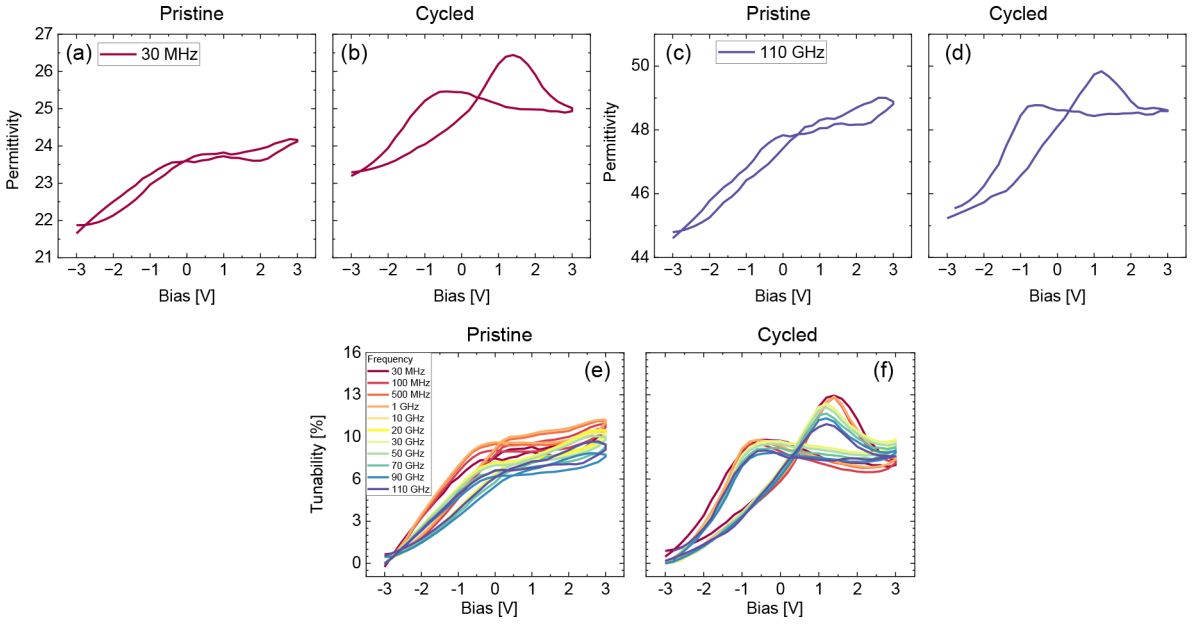


**Figure 5.** $C-V$ characteristics at 30 MHz (a, b) and at 110 GHz (c, d), and tunability versus bias (e, f) of an HZO MFM varactor in the pristine form (a, c, e) and after the wake-up cycling (b, d, f), obtained from the impedance analysis.

The origin of the imprint is most likely due to the accumulation of space charges on one of the capacitor's electrodes, which could increase the pinching of the domain walls[19] and create a Schottky effect.[20] In general, the space charges and defects have a significant influence on the $C-V$ characteristics of thin film ferroelectrics,[20] which could explain why in comparison to $P-V$ characteristics the small-signal $C-V$ characteristics show a more profound imprint. In polycrystalline thin films, like HZO, the grain boundary defects also play a big role.[21] Although the C−V peaks are lying on the coercive voltage values, their origin is in greater extent due to the Schottky effect, caused by the depolarization field of electrodes, that compensates the ferroelectric polarization.[22] Since TiN electrodes are used on both sides of the HZO, electrodes have the same work function. This, together with the fact that the imprint does not disappear upon wake-up, can indicate the formation of an additional layer, where the charge traps are accumulating. This leads to forming of a built-in potential, which shifts the coercive peaks toward higher bias values.

In Figure 4(d) the loss tangent of the varactor is plotted versus bias. The maximum dielectric losses are lying at maximum tuning voltages and are attributed to the leakage currents, which is expected for 10 nm HZO[3] at bias higher than 3 V. The peaks lying in the vicinity of the coercive voltages are due to energy loss on the domain switching and domain-wall movement.[23] The imprint behavior is also evident.

The varactor functionality is described by its tunability ($\tau$), which is defined as

$$\tau = \frac{\varepsilon'(V_c) - \varepsilon'(V_t)}{\varepsilon'(V_c)} \tag{1}$$

where $\varepsilon'(V_c)$ and $\varepsilon'(V_t)$ are real parts of the complex dielectric permittivity at the coercive voltage $V_c$ and at maximum tuning voltage $V_t$, respectively.

In our case the maximum tunability is achieved in the left branch of a $C-V$ curve, between −3 and 1.5 V in the pristine state, and between −3 and 1 V after the full wake-up.

In Figure 4(e) the tunability is plotted versus cycles. It can be seen that upon wake-up the maximum tunability is increasing from 8% to 15%.

## MMWAVE CHARACTERIZATION

During the mmWave characterization, following a de-embedding procedure, the real and imaginary permittivities $\varepsilon'$ and $\varepsilon''$, as well as loss tangent tan $\delta$, were calculated from the real and imaginary parts of the complex transfer impedance $Z_{12}$, using the following relations:

$$\varepsilon' = \frac{-\mathrm{Im}\, Z_{12} \cdot d}{\omega \varepsilon_0 A |Z_{12}|} \tag{2}$$

$$\varepsilon'' = \varepsilon' \cdot \frac{-\mathrm{Re} Z_{12}}{\mathrm{Im}\, Z_{12}} \tag{3}$$

$$\tan \delta = \frac{\varepsilon''}{\varepsilon'} \tag{4}$$

where $Z_{12}$ is a forward transfer impedance, $\omega$ is the frequency, $A$ is the area, and $d$ is the thickness of the capacitor. More details on the derivation of these relations are given in the Supporting Information. Hereinafter we will refer only to the real part of the complex permittivity as "permittivity".

In Figure 5(a)−(d), the $C-V$ characteristics of the ferroelectric HZO MFM varactors are presented at 30 MHz [Figure 5(a), (b)] and at 110 GHz [Figure 5(c), (d)] in the pristine form [Figure 5(a), (c)] and after the wake-up cycling [Figure 5(b), (d)]. It can be seen that the $C-V$ characteristics have the characteristic butterfly shape, as in Figure 4(c), but with a higher proportion of the imprint behavior. It also evident that at higher frequencies the permittivity reaches higher values. Thus, for a better comparison, the $C-V$ characteristics were normalized to tunability and plotted in Figure 5(e) and (f) for pristine and cycled samples,


https://doi.org/10.1021/acsaelm.2c01273
ACS Appl. Electron. Mater. 2023, 5, 189−195

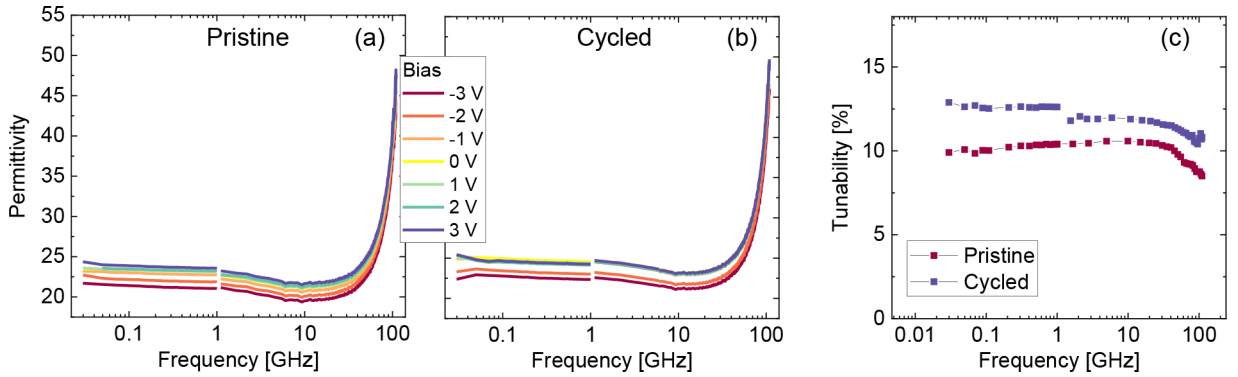


**Figure 6.** Permittivity of the pristine (a) and cycled (b) HZO MFM varactor and corresponding tunabilities (c) plotted in the frequency domain.

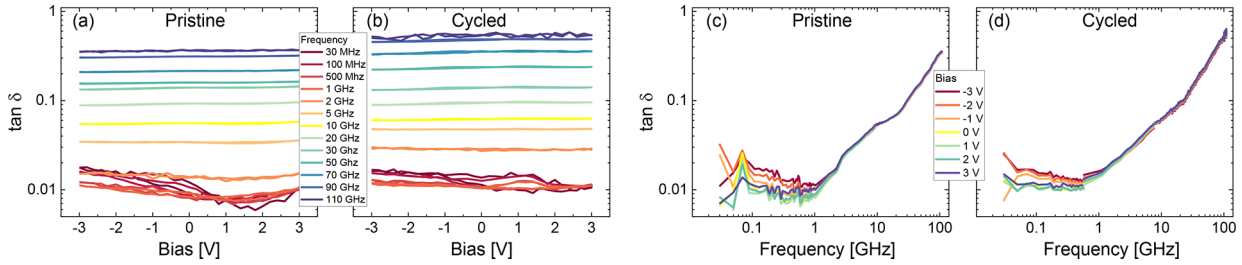


**Figure 7.** tan $\delta$−$V$ characteristics (a, b) at different frequencies and the frequency dependence of tan $\delta$ (c, d) of the HZO MFM varactor in pristine form (a, c), and after the wake-up cycling (b, d), obtained from the impedance analysis.

respectively, where some slight reduction of the tunability upon frequency increase is visible.

In Figure 6(a) and (b) the permittivity is plotted in the frequency domain in logarithmic scale for the pristine and woken-up HZO, respectively. Both plots are composed of measurement data obtained from varactors with different areas. The 30 MHz−1 GHz frequency range was measured using a 900 $\mu m^2$ varactor, whereas the 1−110 GHz range was measured using a 4 $\mu m^2$ varactor. The reason for split measurements is due to the different cutoff frequencies of the varactors and is explained in more detail in the Supporting Information. The permittivity data show a good convergence for such a large area difference. In the frequency range of 30 MHz−40 GHz a slight reduction of permittivity is visible for both pristine and cycled samples, which could be associated with the dielectric relaxation. At a frequency higher than 40 GHz, the permittivity shows a strong increase up to $\varepsilon' = 49$ and $\varepsilon' = 50$ at 110 GHz in the pristine and cycled state, respectively. Such an increase is probably an artifact caused by the skin effect[17] arising from the parasitic inductance of a thin shunting contact line, which was not fully compensated by the de-embedding (see the Supporting Information). Also, the increasing permittivity could be caused by the parasitic capacitance of the substrate as a result of the absence of a proper metal shielding. Therefore, the exact values of permittivity are only tangible up to 40 GHz. Upon the bias sweep, the permittivity shifts toward higher or lower values in the entire frequency range.

In Figure 6(c), the tunability is plotted versus frequency both for pristine and cycled HZO. At 30 MHz, the maximum values of tunability for pristine and cycled samples reach 10% and 12.9%, respectively. Upon increasing frequency, the tunability of the pristine sample experiences a slight increase up to 10.5% at 20 GHz, showing a smooth transition between measurements at different frequency ranges, and then reduces up to 8.5% at 110 GHz. The tunability of the cycled samples, however, demonstrates a worse transition and shows a reduction from 12.9% at 30 MHz up to 11% at 110 GHz. In general, however, it can be concluded that the tunability is fairly stable, given the huge frequency range.

It should also be noted that during the RF characterization the bias was swept very slowly with 0.5 V steps, and the duration of each measurement took 10 s, which indicates the stability of the varactor tuning. Considering the imprint behavior, these ferroelectric varactors can potentially be used in nonvolatile capacitive crossbar arrays for in-memory computing.[19]

In Figure 7(a) and (b) the tan $\delta$−$V$ characteristics are presented for pristine and cycled samples, respectively. Unlike in Figure 4(d), the loss tangent peaks are only present at coercive fields, which can be explained by the RF measurement setup, where the real part of the impedance is less sensitive to the leakage currents. At frequencies above 1 GHz, the peaks are not visible at all, which can be explained by the small area of the varactor (4 $\mu m^2$) used for characterization in this frequency range. Because of the small number of domains, they do not generate sufficiently strong displacement currents during the switching process that could sufficiently contribute to the formation of the corresponding peaks. Hence, the dielectric and extrinsic losses predominate over the ferroelectric ones. This is also visible in Figure 7(c) and (d), where the frequency dependence of tan $\delta$ is plotted for pristine and cycled HZO, respectively. In the lower frequency range (<1 GHz) the variation of the tan $\delta$ upon bias is more profound than at higher frequencies. In the frequency range of 1−110 GHz, the loss tangent showed an increase upon frequency from 0.01 up to 0.35 in the pristine state and from 0.01 to 0.67 after wake-up.

This kind of increase is linear in the frequency domain, which could be originating from the intrinsic losses due to



https://doi.org/10.1021/acsaelm.2c01273
ACS Appl. Electron. Mater. 2023, 5, 189−195

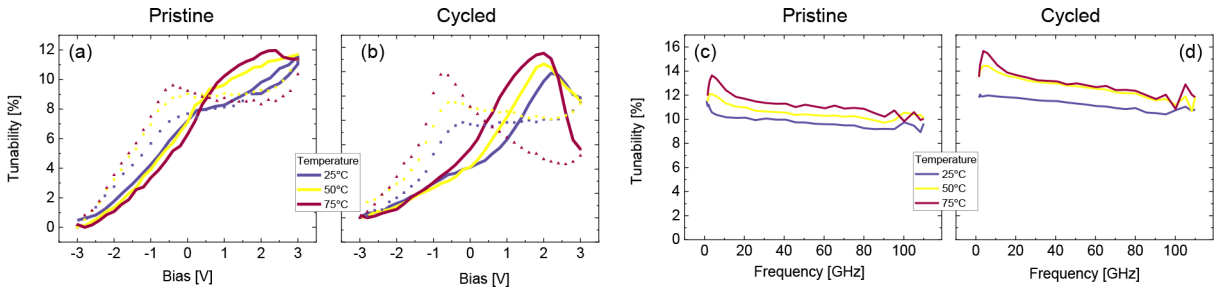


**Figure 8.** Tunability vs bias (a, b) and tunability vs frequency (c, d) at different temperatures for pristine and cycled samples, respectively.

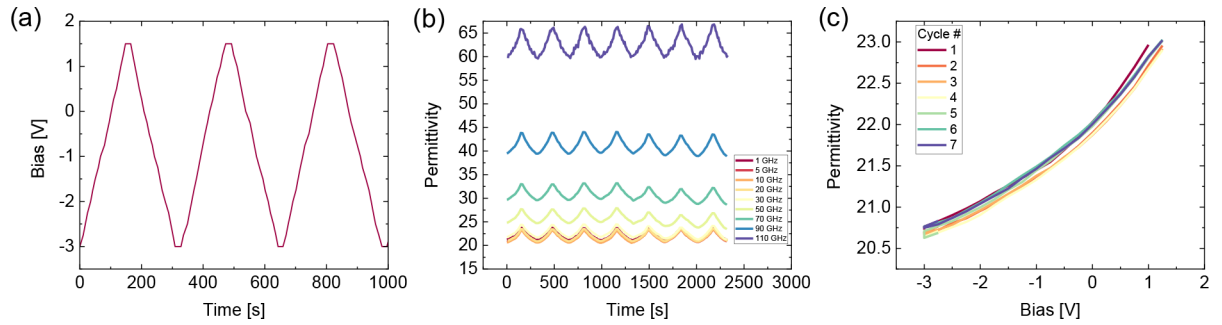


**Figure 9.** Applied bias range (a) and permittivity (b) in the time domain and resulting $C-V$ characteristics (c) at 1 GHz upon multiple cycles in the varactor regime.

phonon interaction[24] or universal relaxation law.[25] In the case of parallel-plate varactors, the series electrode resistance plays a significant role in the loss tangent.[26] Such a high linear increase is most likely a result of series shunting resistance, which was not fully de-embedded (see discussion in the Supporting Information).

We have also performed the measurements at elevated temperatures of 50 and 75 °C (Figure 8). $C-V$ characteristics of both pristine [Figure 8(a)] and cycled [Figure 8(b)] samples reveal an increase of tunability with temperature caused by enhancing of the FE behavior and a decrease of an imprint and Schottky behavior. This can be explained by an increased mobility of the charge carriers on the interface layer, where the Schottky contact is formed, allowing higher displacement currents. In Figure 8(c) and (d) the tunabilities of the pristine and cycled samples are plotted in the frequency domain, where the tunability is stable in the whole frequency range.

For the demonstration of a continuous functionality in the varactor regime,[3] we have swept the bias between −3 and 1.5 V [Figure 9(a)] continuously 7 times. The resulting permittivity variation in time domain is depicted in Figure 9(b) for different frequencies, where a stable tuning can be observed. In Figure 9(c) the $C-V$ characteristics at 1 GHz are extracted, demonstrating stable tuning behavior with over 7 sweeps. The tuning behavior also demonstrates a high degree of linearity, which is beneficial for analog applications.

## CONCLUSION

In this paper we demonstrated a broadband RF characterization of the MFM hafnium zirconium oxide thin film varactor, integrated into the BEoL of a 180 nm CMOS SOI technology. At low frequencies of 1 kHz the varactor shows a strong imprint behavior, which can be attributed to the formation of a charge trap layer near one of the electrodes, that increases the pinning of the domain walls and creates a Schottky effect. The maximum tunability at low frequency reaches 8% in the pristine state and 15% after the wake-up, caused by cycling 100 000 times at 1 kHz frequency. During the frequency sweep between 30 MHz and 110 GHz and the bias sweep between −3 and 3 V, the varactor has shown more profound imprint behavior than at low frequency. At 30 MHz maximum tunability has changed to 10% in the pristine state and 13% after the wake-up. The tunability showed a good stability in the entire frequency range, both at room temperature and up to 75 °C, and experiences only a slight decrease of 2% in the 40−110 GHz frequency range. During the multiple cycles in the varactor regime, the device has demonstrated a stable and linear tuning, which is advantageous for the analog applications.

## ASSOCIATED CONTENT

### Supporting Information

The Supporting Information is available free of charge at https://pubs.acs.org/doi/10.1021/acsaelm.2c01273.

More detailed information about de-embedding and permittivity extraction, including co-simulation (PDF)

## AUTHOR INFORMATION

### Corresponding Authors

**Sukhrob Abdulazhanov** − *Center Nanoelectronic Technologies, Fraunhofer IPMS, 01109 Dresden, Germany;* orcid.org/0000-0001-7305-2811; Phone: +49 0351 26073202; Email: sukhrob.abdulazhanov@ipms.fraunhofer.de

**Gerald Gerlach** − *Institute of Solid State Electronics, TU Dresden, 01067 Dresden, Germany;* Email: gerald.gerlach@tu-dresden.de

### Authors

**Quang Huy Le** − *Center Nanoelectronic Technologies, Fraunhofer IPMS, 01109 Dresden, Germany*



https://doi.org/10.1021/acsaelm.2c01273
ACS Appl. Electron. Mater. 2023, 5, 189−195

**Dang Khoa Huynh** − *Center Nanoelectronic Technologies, Fraunhofer IPMS, 01109 Dresden, Germany*
**Defu Wang** − *Center Nanoelectronic Technologies, Fraunhofer IPMS, 01109 Dresden, Germany*
**David Lehninger** − *Center Nanoelectronic Technologies, Fraunhofer IPMS, 01109 Dresden, Germany*
**Thomas Kämpfe** − *Center Nanoelectronic Technologies, Fraunhofer IPMS, 01109 Dresden, Germany*

Complete contact information is available at: https://pubs.acs.org/10.1021/acsaelm.2c01273

### Notes

The authors declare no competing financial interest.

## ■ ACKNOWLEDGMENTS

This work has received funding from the ECSEL Joint Undertaking (JU) under grant agreement No. 783127. The JU receives support from the European Union's Horizon 2020 research and innovation program and France, Germany, Austria, Poland, Portugal, and Spain. The fabrication was supported by the X-FAB foundry group. The authors would also like to thank Hannes Maehne for the support during the design and fabrication.

## ■ REFERENCES

(1) Böscke, T. S.; Müller, J.; Bräuhaus, D.; Schröder, U.; Böttger, U. Ferroelectricity in hafnium oxide thin films. *Appl. Phys. Lett.* **2011**, *99*, 102903.
(2) Mart, C.; Abdulazhanov, S.; Czernohorsky, M.; Kämpfe, T.; Lehninger, D.; Falidas, K.; Eslinger, S.; Kuhnel, K.; Oehler, S.; Rudolph, M.; Wiatr, M.; Kolodinski, S.; Seidel, R.; Weinreich, W.; Eng, L. M.*Energy Harvesting in the Back-End of Line with CMOS Compatible Ferroelectric Hafnium Oxide 2020 IEEE International Electron Devices Meeting (IEDM)*; *12122020*; pp 26.3.1−26.3.4.
(3) Abdulazhanov, S.; Lederer, M.; Lehninger, D.; Mart, C.; Ali, T.; Wang, D.; Olivo, R.; Emara, J.; Kampfe, T.; Gerlach, G. Tunability of Ferroelectric Hafnium Zirconium Oxide for Varactor Applications. *IEEE Trans. Electron Devices* **2021**, *68*, 5269−5276.
(4) Lehninger, D.; Olivo, R.; Ali, T.; Lederer, M.; Kämpfe, T.; Mart, C.; Biedermann, K.; Kühnel, K.; Roy, L.; Kalkani, M.; Seidel, K. Back−End−of−Line Compatible Low-Temperature Furnace Anneal for Ferroelectric Hafnium Zirconium Oxide Formation. *physica status solidi (a)* **2020**, *217*, 1900840.
(5) Dragoman, M.; Aldrigo, M.; Modreanu, M.; Dragoman, D. Extraordinary tunability of high-frequency devices using Hf0.3Zr 0.7O2 ferroelectric at very low applied voltages. *Appl. Phys. Lett.* **2017**, *110*, 103104.
(6) Dragoman, M.; Modreanu, M.; Povey, I. M.; Iordanescu, S.; Aldrigo, M.; Romanitan, C.; Vasilache, D.; Dinescu, A.; Dragoman, D. Very large phase shift of microwave signals in a 6 nm HfxZr1−xO2 ferroelectric at ± 3 V. *Nanotechnology* **2017**, *28*, 38LT04.
(7) Dragoman, M.; Modreanu, M.; Povey, I.; Iordanescu, S.; Aldrigo, M.; Dinescu, A.; Vasilache, D.; Romanitan, C. 2.55 GHz miniaturised phased antenna array based on 7 nm-thick HfxZr1 − xO2 ferroelectrics. *Electron. Lett.* **2018**, *54*, 469−470.
(8) Abdulazhanov, S.; Le, Q. H.; Huynh, D. K.; Wang, D.; Lederer, M.; Olivo, R.; Mertens, K.; Emara, J.; Kämpfe, T.; Gerlach, G. RF-Characterization of HZO Thin Film Varactors. *Crystals* **2021**, *11*, 980.
(9) Lin, B.; Choe, G.; Hur, J.; Khan, A. I.; Yu, S.; Wang, H.*Experimental RF Characterization of Ferroelectric Hafnium Zirconium Oxide Material at GHz for Microwave Applications. 2021 Device Research Conference (DRC)*; *6202021*; pp 1−2.
(10) Abdulazhanov, S.; Le, Q. H.; Huynh, D. K.; Wang, D.; Gerlach, G.; Kämpfe, T.*A mmWave Phase Shifter Based on Ferroelectric Hafnium Zirconium Oxide Varactors 2019 IEEE MTT-S International Microwave Workshop Series on Advanced Materials and Processes for RF and THz Applications (IMWS-AMP)*; pp 175−177.
(11) Abdulazhanov, S.; Le, Q. H.; Huynh, D. K.; Wang, D.; Gerlach, G.; Kämpfe, T.*A Tunable mmWave Band-Pass Filter Based on Ferroelectric Hafnium Zirconium Oxide Varactors 2019 IEEE MTT-S International Microwave Workshop Series on Advanced Materials and Processes for RF and THz Applications (IMWS-AMP)*; pp 46−48.
(12) Mannequin, C.; Gonon, P.; Vallée, C.; Bsiesy, A.; Grampeix, H.; Jousseaume, V. Dielectric relaxation in hafnium oxide: A study of transient currents and admittance spectroscopy in HfO 2 metal-insulator-metal devices. *J. Appl. Phys.* **2011**, *110*, 104108.
(13) Esro, M.; Vourlias, G.; Somerton, C.; Milne, W. I.; Adamopoulos, G. High-Mobility ZnO Thin Film Transistors Based on Solution-processed Hafnium Oxide Gate Dielectrics. *Adv. Funct. Mater.* **2015**, *25*, 134−141.
(14) Zhao, C. Z.; Taylor, S.; Werner, M.; Chalker, P. R.; Gaskell, J. M.; Jones, A. C. Frequency dispersion and dielectric relaxation of La[sub 2]Hf[sub 2]O[sub 7]. *Journal of Vacuum Science & Technology B: Microelectronics and Nanometer Structures* **2009**, *27*, 333.
(15) Zhao, C.; Zhao, C. Z.; Werner, M.; Taylor, S.; Chalker, P. Dielectric relaxation of high-k oxides. *Nanoscale Res. Lett.* **2013**, *8*, 456.
(16) Vo, T. T.; Lacrevaz, T.; Flechet, B.; Farcy, A.; Morand, Y.; Blonkowski, S.; Torres, J.; Defay, E.*In-situ Microwave Characterization of Medium−k $HfO_2$ and High−k STODielectrics for MIM Capacitors Integrated in Back-End of Line of IC. 2007 Asia-Pacific Microwave Conference*; 2007; pp 1−4.
(17) Lourandakis, E.*On-Wafer Microwave Measurements and De-embedding*; Microwave design; Artech House: Boston, 2016.
(18) Schenk, T.; Yurchuk, E.; Mueller, S.; Schroeder, U.; Starschich, S.; Böttger, U.; Mikolajick, T. About the deformation of ferroelectric hystereses. *Applied Physics Reviews* **2014**, *1*, 041103.
(19) Hur, J.; Luo, Y.-C.; Lu, A.; Wang, T.-H.; Li, S.; Khan, A. I.; Yu, S. Nonvolatile Capacitive Crossbar Array for In−Memory Computing. *Advanced Intelligent Systems* **2022**, *4*, 2100258.
(20) Brennan, C. J. Characterization and modelling of thin-film ferroelectric capacitors using C-V analysis. *Integr. Ferroelectr.* **1992**, *2*, 73−82.
(21) Ogata, N.; Ishiwara, H. A Model for High Frequency C-V Characteristics of Ferroelectric Capacitors. *IEICE Transactions on Electronics* **2001**, *84*, 777−784.
(22) Mehta, R. R.; Silverman, B. D.; Jacobs, J. T. Depolarization fields in thin ferroelectric films. *J. Appl. Phys.* **1973**, *44*, 3379−3385.
(23) Liu, G.; Zhang, S.; Jiang, W.; Cao, W. Losses in Ferroelectric. *science & engineering. R, Reports: a review journal* **2015**, *89*, 1−48.
(24) Vorobiev, A.; Rundqvist, P.; Khamchane, K.; Gevorgian, S. Microwave loss mechanisms in Ba0.25Sr0.75TiO3 thin film varactors. *J. Appl. Phys.* **2004**, *96*, 4642−4649.
(25) Gevorgian, S.*Ferroelectrics in microwave devices, circuits and systems: Physics, modeling, fabrication and measurements*; Springer Science & Business Media, 2009.
(26) Tagantsev, A. K.; Sherman, V. O.; Astafiev, K. F.; Venkatesh, J.; Setter, N. Ferroelectric Materials for Microwave Tunable Applications. *Journal of Electroceramics* **2003**, *11*, 5−66.